Unsteady ripple generation on steep gravity–capillary waves

By LEI JIANG[1]†, HUAN-JAY LIN[1],
WILLIAM W. SCHULTZ[1] AND MARC PERLIN[2]

[1]Department of Mechanical Engineering and Applied Mechanics, University of Michigan

[2]Department of Naval Architecture and Marine Engineering,
University of Michigan Ann Arbor, Michigan 48109, USA

Parasitic ripple generation on short gravity waves (4 cm to 10 cm wavelengths) is examined using fully nonlinear computations and laboratory experiments. Time-marching simulations show sensitivity of the ripple steepness to initial conditions, in particular to the crest asymmetry. Significant crest fore–aft asymmetry and its unsteadiness enhance ripple generation at moderate wave steepness, e.g. *ka* between 0.15 and 0.20, a mechanism not discussed in previous studies. The maximum ripple steepness (in time) is found to increase monotonically with the underlying (low-frequency bandpass) wave steepness in our simulations. This is different from the sub- or super-critical ripple generation predicted by Longuet-Higgins (1995). Unsteadiness in the underlying gravity–capillary waves is shown to cause ripple modulation and an interesting 'crest-shifting' phenomenon – the gravity–capillary wave crest and the first ripple on the forward slope merge to form a new crest. Including boundary layer effects in the free-surface conditions extends some of the simulations at large wave amplitudes. However, the essential process of parasitic ripple generation is nonlinear interaction in an inviscid flow. Mechanically generated gravity–capillary waves demonstrate similar characteristic features of ripple generation and a strong correlation between ripple steepness and crest asymmetry.

1. Introduction

Ripple generation on steep gravity and gravity–capillary waves has received much attention in recent years because of remote-sensing applications. The ripple wavelength and steepness affect the energy distribution in the wave spectrum, and the correspondence between ripple steepness and the underlying (low-frequency bandpass) wave steepness is a key in estimating the sea state from Synthetic Aperture Radar (SAR) returns. Experimental studies on this subject began with observations by Cox (1958) of ripples riding ahead of wave crests in wind-generated waves. More recent laboratory studies include Chang, Wagner & Yuen (1978), Yermakov *et al.* (1986), Ebuchi, Kawamura & Toba (1987), and Perlin, Lin & Ting (1993). A recent study by Longuet-Higgins (1992*b*) also suggests parasitic ripples generate vorticity and enhance wave dissipation. Lin & Perlin (1999) measure vorticity generated beneath gravity–capillary waves with capillary ripples present.

† Present address: Intel Corp. RA1-305, 5200 N. E. Elam Young Pkwy., Hillsboro, OR 97124, USA.

One physical mechanism of this interesting and important phenomenon is clarified in the theory of Longuet-Higgins (1963, hereafter referred to as LH63) where the surface-tension force acting near the crest of a steep gravity wave produces ripples upstream of the crest (as well as longer waves downstream). For simplicity, Longuet-Higgins used the Stokes gravity wave as the zeroth-order solution to supply the large crest curvature necessary for ripple excitation. A nearly steady solution is then obtained by balancing the energy input to the ripples with viscous dissipation; no feedback from the ripples to the underlying wave is considered. The Longuet-Higgins solutions are therefore fundamentally different from the steady, inviscid, periodic solutions found numerically by Schwartz & Vanden-Broeck (1979) and by Chen & Saffman (1979, 1980). These steady solutions have more prominent ripples in the wave trough than on the forward face. LH63 and Longuet-Higgins (1995, hereafter referred to as LH95) recognized that the nonlinearity of the underlying gravity waves is the essence of upstream ripple generation. This is justified by comparison with Cox (1958) and with later experimental studies.

Both Chang *et al.* (1978) and Yermakov *et al.* (1986) found that LH63 correctly predicts the ripple wavelengths and decay while underestimating the maximum ripple steepness θ_r for given underlying wave steepness ka. This is again shown in Perlin *et al.* (1993) with both spatial and temporal measurements. Significant ripples often appear at moderate wave steepness ($0.15 < ka < 0.25$) in the experiments whereas LH63 predicts much smaller ripples. However, LH95 cautioned against comparison between the quasi-steady theory and the undoubtedly unsteady experiments that usually measure an instantaneous wave profile or a temporal wave height at a fixed location. Laboratory studies using mechanical wavemakers make direct comparison even more ambiguous as the waves and ripples decay quickly downstream. An accurate model comparison requires a full treatment in time with a semi-infinite domain. Here we do time marching, but unfortunately with periodic boundary conditions for computational economy.

In this study, we investigate in detail the complete ripple generation process. Similarly to the aforementioned experiments, we use a mechanical shaker to generate short gravity–capillary waves upon which parasitic ripples are excited near the crest. The flap-type wavemaker used here reduces the disturbances that might be introduced by a plunger wavemaker. Simulations of gravity–capillary waves are based on potential flow with the viscous effect simply modelled by a damping term in the dynamic free-surface condition. Watson & Buchsbaum (1996) proposed a weakly nonlinear approach to study interaction between ripples and longer waves for unsteady ripple generation. Our time simulation herein is based on a fully nonlinear formulation.

Our results reinforce the conclusion of LH63 that the localized crest curvature of the underlying wave is the source of the ripples. The disagreement between laboratory experiments, the numerical results of Dommermuth (1994), and the theory of LH63 is probably due to the unsteadiness and the fore–aft asymmetry of the underlying waves. These two factors are particularly important to parasitic ripple generation at moderate ka. In fact, asymmetry is clearly present in the time series of the wave elevation measured by Cox (1958). We find that an inviscid model adequately describes these effects in ripple generation. The viscous effect is relatively insignificant. However, the viscous layer beneath capillary ripples is important during short-wave breaking, such as the spilling breakers observed by Duncan *et al.* (1994). In some simulations, we also observe numerical divergence similar to the singularity formation in the spilling breaker simulation (Schultz, Huh & Griffin 1994). This divergence is due to the breakdown of the inviscid model, not the spectral boundary-integral scheme.

Most recently, Fedorov & Melville (1998) presented a method for calculating steady parasitic ripples on gravity–capillary waves with wind forcing. Including this important parameter results in two classes of waves corresponding to different phase angles between the wind pressure and the underlying wave. They also presented experimental results on wave spectra and ripple steepness. With wind forcing, the steepness of capillary ripples can reach significant values even for steady gravity–capillary waves. An asymmetric wind pressure distribution also enhances the crest asymmetry of the generated gravity–capillary wave. However, wind effect is beyond the scope of the present study.

In an improved treatment of parasitic ripple generation (LH95), Longuet-Higgins found a critical underlying wave steepness ka_{cr} beyond which the ripple steepness decreases with increasing ka. This conclusion is based on the blocking effect of large ka through an effective gravitational acceleration. It is similar to the trapping of free gravity waves between two 'caustics' on a long wave (Phillips 1981; Shyu & Phillips 1990) and the blockage of a free capillary wave packet by a gravity wave (Woodruff & Messiter 1994). In parasitic ripple experiments, however, Yermakov *et al.* (1986) observed a monotonic increase of the maximum ripple steepness θ_r with ka. Our numerical results agree with Yermakov *et al.* (1986) but our experiments cannot confirm this because of the limited ka required to retain a one-dimensional surface. In our experiments, the ripple steepness is more sensitive to the crest asymmetry than to the steepness of the underlying wave. A crest-merging interaction between ripples and the primary wave is found in both experiments and numerical results, and it resembles the modulation between subcritical waves and supercritical waves. However, the underlying mechanism is not due to the blockage of ripples by large ka, but rather due to the nonlinear recurrence of fore–aft crest asymmetry.

This paper is organized as follows. A Cauchy-integral method applied to a time-marching simulation is described in §2. Improved experimental techniques are discussed in §3. Numerical results are presented in §4 on crest asymmetry, large ripple steepness, and ripple modulation. We present our experimental findings in §5. The unique features of unsteady ripple generation are summarized in §6.

2. Numerical strategy with the Cauchy integral method

Large Reynolds number gravity–capillary waves indicate potential flow with the viscous effect confined to a thin boundary layer near the free surface. We further assume a deep-water condition and periodicity in the horizontal x-direction. The chosen length and time scales are k^{-1} and $(gk)^{-1/2}$, respectively. Here k represents the primary wavenumber and g represents the gravitational acceleration. Then, the dimensionless wavelength λ and the linear wave period T are both 2π. The surface tension and viscous effects are represented by the inverse Bond number κ and Reynolds numbers Re:

$$\kappa = \frac{\sigma k^2}{\rho g}, \quad Re = \frac{g^{1/2}k^{-3/2}}{v},$$

where σ is the surface tension coefficient and v is the kinematic viscosity. We apply a fully nonlinear numerical scheme based on the Cauchy integral theorem for complex potentials (Vinje & Brevig 1981) to describe the two-dimensional potential flow with a free surface. The physical domain, with $z = x + iy$ where y is measured vertically upward from the undisturbed free surface, is mapped to an approximate unit circle using the conformal transformation: $\zeta = e^{-iz}$. This satisfies the deep-water and

periodic boundary conditions. The Lagrangian forms of the kinematic and dynamic conditions on the free surface $\xi = x + iy$ are

$$\frac{D\xi}{Dt} = \frac{dw^*}{d\xi},\tag{2.1}$$

$$\frac{D\phi}{Dt} = -y + \frac{1}{2}\left|\frac{dw^*}{d\xi}\right|^2 - \kappa\frac{x'y'' - x''y'}{(x'x' + y'y')^{3/2}} + \frac{2}{Re}\phi'',\tag{2.2}$$

where $w(\xi, t) = \phi + i\psi$ is the unknown complex potential on the free surface. Here, D/Dt represents the material derivative and * denotes the complex conjugate. In the expression for surface curvature, primes represent derivatives with respect to a free-surface arclength parameter. The discretized velocity potential $w(\zeta_j)$ is determined by the Cauchy integral equation

$$\oint_{\partial\Omega} \frac{w(\xi)}{\xi - \zeta_j}d\xi = i\alpha w(\zeta_j)\tag{2.3}$$

at the jth node on the free surface. Here, $\alpha = \pi$ is the included angle of a smooth surface. The integral equation (2.3) is then converted to an algebraic system for $w(\xi)$. A cardinal function representation of w is used to evaluate the integrand spectrally and remove the singularity in the integral (Schultz *et al.* 1994). All derivatives in the free-surface conditions are also taken spectrally in the conformed space. More details of the method are described in Schultz *et al.* (1994).

Although the boundary layer dynamics beneath the free surface are not modelled, we model the viscous stress in the boundary layer as described by the last term in (2.2). A similar viscous term in the dynamic boundary condition is also applied in Miksis, Vanden-Broeck & Keller (1982) to rising bubbles. Dommermuth (1994) also includes a term proportional to ξ'' in (2.1), representing the contribution from the tangential shear stress in the boundary layer. Our numerical experiments show this additional viscous term in (2.1) has no qualitative effect on ripple generation. This *ad-hoc* model is chosen only to model the linear damping effect as the viscous boundary layer approach breaks down for very large ripple curvature. More detailed discussion of the boundary-layer analysis can be found in Lundgren (1989) and Longuet-Higgins (1992*a*).

We restrict the number of nodes N to powers of 2 and use the FFT to spectrally estimate the spatial derivatives in the free-surface conditions. Initially, markers z_j are distributed uniformly along the free surface. To avoid clustering of nodes around the wave crest, we fix the horizontal position of the markers at later time steps (Schultz *et al.* 1998). The algebraic equations obtained from (2.3) are solved iteratively for the unknown part of the complex potential $w(\zeta_j)$ at each later time step. Equations (2.1) and (2.2) are then applied to the markers with a fourth-order modified Hamming predictor-corrector method to update ϕ_j and z_j. Both marching and iteration error tolerances are set at 10^{-10}. The error in the normalized energy is constant to within 10^{-10} when the dissipation is absent as measured by

$$E = E_p + E_k + E_s = \frac{1}{2}\int_0^{2\pi}\eta^2 dx + \frac{1}{2}\int_0^{2\pi}\phi\frac{\partial\psi}{\partial s}ds + \kappa\left[\int_0^{2\pi}ds - 2\pi\right].$$

These three terms represent potential energy density E_p, kinetic energy density E_k, and surface-tension energy density E_s.

Four types of initial conditions are applied to study their effect on ripple strength: a linear, a third-order and a fifth-order Stokes gravity wave solution (Fenton 1985),
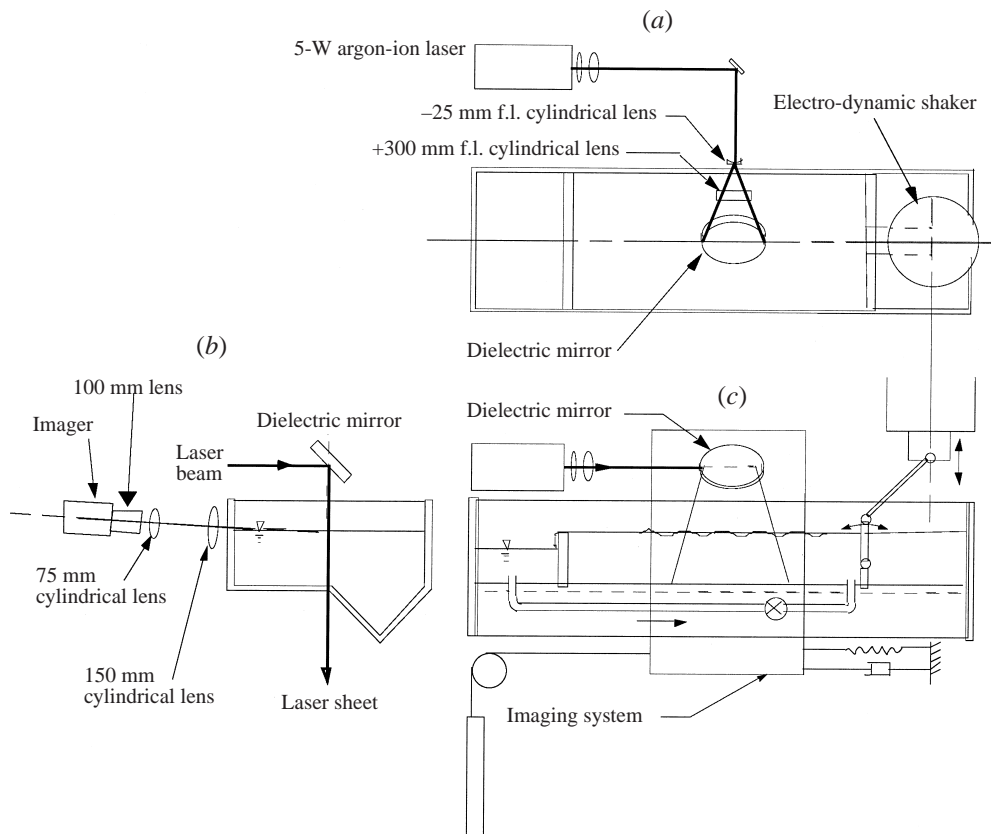
FIGURE 1. The experimental setup for wave-profile measurements:
(*a*) top view, (*b*) end view, (*c*) side view.

and a third-order solution for a gravity–capillary wave (Wehausen & Laitone 1960). Additional information about the time-marching simulation is presented in §4.

3. Experimental apparatus and measurement techniques

Gravity–capillary waves with frequencies between 4.21 Hz and 6.70 Hz are generated by a flap-type wavemaker within a 3.0 m long, 0.3 m wide, closed water channel (figure 1). A minimum water depth of 8 cm is chosen to satisfy the deep-water criterion for this frequency range. The movable flap wavemaker is hinged to a fixed vertical plate about 5 cm beneath the undisturbed free surface and is driven by a sinusoidal signal with excellent repeatability: feedback of its displacement matches the primary frequency input signal, while other (harmonic) frequency components have less than 0.5% the amplitude of the primary frequency component. The generated waves are of moderate ka (0.13 to 0.24). At high frequencies, three-dimensional effects become significant near the wavemaker for $ka > 0.24$. The wavemaker can generate higher wave amplitude for lower-frequency waves (4.21 Hz), but strong modulation occurs possibly due to Benjamin–Feir instability.

The associated experimental apparatus includes: a 5 W argon-ion laser; attendant optics (two-spherical lenses, two cylindrical lenses, and three dielectric mirrors); a programmable shaker/wave maker with feedback; signal generation and data acqui-

sition system; and a high-speed, 8-bit video system with intensified imager and imaging optics. The motion of the piston shaker (that drives the flap-type wavemaker) is controlled by a Power Macintosh 7100 computer equipped with National Instruments' data-acquisition boards/LabVIEW software, and the Metrowerks C/C++ compiler. Programs are written for a synchronous multi-channel signal/trigger generation, such that the host computer can automatically control the motion of the wavemaker and the trigger to start the imaging system recording. A laser sheet, generated by the argon-ion laser and expanded by a cylindrical lens, is created perpendicular to the wave fronts. Fluorescent dye (fluorescein) is added to the water so that the intersection of the laser sheet and the free surface forms a sharp intensity discontinuity in the image. The measured surface tension for clean water is $72\,\mathrm{dyne\,cm^{-1}}$ at room temperature. The dye decreases the surface tension by approximately $1\,\mathrm{dyne\,cm^{-1}}$.

A high-speed-video system is used for recording time-series images. The image recording device is a Kodak Ektapro CID (charge-injection device) intensified imager and controller coupled to an Ektapro EM 1012 processor. The imager is located on a (horizontal) precision rail and may be attached to a pulley/weight and spring/damping system (figure 1). The weight, damping, and spring are adjusted such that the imager moves at approximately the wave phase velocity. The purpose of this apparatus is to measure the wave profile as it propagates downstream. The optical axis is oriented 15° above horizontal to remove the meniscus effect (see end view in figure 1). There is no significant image distortion in either direction. The irregular tank bottom is for optical measurements below the surface (Lin & Perlin 1999) that are not made here. For the short waves studied here, the bottom has no effect. The Ektapro EM 1012 processor system has the capacity to record 408 image frames in RAM with two connected imagers with an adjustable framing rate from 50 to 1000 Hz. Once a set of images is stored in the processor, it is downloaded via a standard GPIB interface to the computer for analysis. An edge-detection routine is sometimes used to process the data. The location of the water surface elevation, for any horizontal position in the image, is defined by the point at which the grey-scale image provides greatest contrast (intensity gradient).

To examine the fine-scale features of the wave profiles, a pair of cylindrical lenses with a horizontally oriented axis is installed in front of the 100 mm focal-length Canon lens mounted on the imager. A 10 mm extension tube is attached to the imager. One cylindrical lens with a 62.5 mm focal length is mounted on an optical rail near the camera lens, while a second lens with a 150 mm focal length is located approximately 300 mm (adjustable) from the camera lens. These two cylindrical lenses can produce a vertically magnified virtual image located at the position of the original object. The image is 239×192 pixels. The spatial resolution determined using a precise resolution target is typically 0.4 mm $\times$ 0.05 mm, i.e. an approximately eight-fold magnification in the vertical direction relative to the horizontal dimension. In practice, the camera lens is first focused on the illuminated free surface, and then the second cylindrical lens is focused to produce the virtual image. A horizontal slot with a controllable opening provides aperture control on the cylindrical lenses (especially the lens nearest the object), restricting the lens usage to the central region where the distortion is the smallest. The induced distortion (albeit small) and other details are discussed in Perlin *et al.* (1993).

4. Numerical results

We confirm the spatial convergence of the time-marching computations by using four different grids: 64, 128, 256, and 512 nodes per primary wavelength. The devel-

opment of large surface curvature and steep slope, however, often leads to divergence for large time unless the error requirement is significantly relaxed. In these situations, the computation is repeated with smaller time steps until no improvement can be achieved.

4.1. *Unsteady gravity wave and ripple generation*

We first study inviscid ripple development on an initially sinusoidal wave (initial free-surface boundary condition of $\xi = ka \cos kx$ and $\phi = ka \sin kx$) with $\kappa = 0.07$ ($\lambda = 6.5$ cm) and $ka = 0.20$. The linear wave initial condition is partially chosen to capture the unsteady motion for laboratory conditions with a flap-type wavemaker following a sinusoidal motion.

The wave profiles at later times are shown in figure 2 in a coordinate system moving with the linear phase speed $c = [g(1+\kappa)/k]^{1/2}$. For clarity, two wavelengths are shown although we only calculate one. The dots in figure 2 represent the instantaneous locations of the maximum negative curvature Γ (same sign as the crest curvature). The wave first becomes both vertically and horizontally asymmetric, i.e. the crest rises and tilts forward. A wave with horizontal symmetry would have a symmetric elevation about a vertical axis at the crest. The maximum curvature grows with time, and its location also moves from the wave crest to the forward face. Ripples on the steepening forward face become obvious after only one wave period (the eighth profile from the top). Inclusion of the damping term in (2.2) has little effect on the ripple steepness and the asymmetry for the moderate waves shown in figure 2. The parasitic ripple generation is therefore essentially inviscid and irrotational, as alluded to in LH63.

The ripple growth in figure 2 continues until the inviscid computation fails after two wave periods. It will be shown later (§ 4.3) that the computational failure is caused by steep wave slope near the crest and large surface curvature in the ripple trough where the viscous effect should be included. However, the wave profiles in figure 2 are fully resolved and represent the main features of the inviscid ripple generation.

Simulations of other wavelengths demonstrate the same characteristic features: occurrence of maximum curvature on the forward face and fore–aft crest asymmetry. The ripple steepness is significantly larger than the quasi-steady prediction of LH63 and LH95. This qualitatively agrees with the experiments by Perlin *et al.* (1993) and the simulation of Dommermuth (1994) where noticeable fore–aft asymmetry and similar strong ripples are present. The solution of Longuet-Higgins has a more symmetric primary crest even though the ripple presence is asymmetric about the crest.

It is also worth emphasizing that strong fore–aft asymmetry develops before ripples are observed. The maximum slope on the forward face eventually reaches 0.60 in figure 2, while the maximum rear slope oscillates between 0.16 and 0.26. Longuet-Higgins (1978) found that a local instability of the limiting crest form (120° crest for a gravity wave) leads to an asymmetric crest and a 'toe' on the forward face (Longuet-Higgins & Cleaver 1994; Longuet-Higgins, Cleaver & Fox 1994). This instability, however, only develops near a limiting Stokes wave ($ka > 0.40$), and Stokes waves are stable to superharmonic disturbances at moderate steepness. Therefore the asymmetry mechanism shown herein is qualitatively different from the instability of limiting Stokes waves.

The role of symmetry can be further understood by revisiting the calculations by Perlin *et al.* (1993) using the formulation of Schwartz & Vanden-Broeck (1979). While their formulation is fully nonlinear, steadiness and fore–aft symmetry are assumed. The solutions found by Perlin *et al.* (1993), as expected, have much smaller ripple
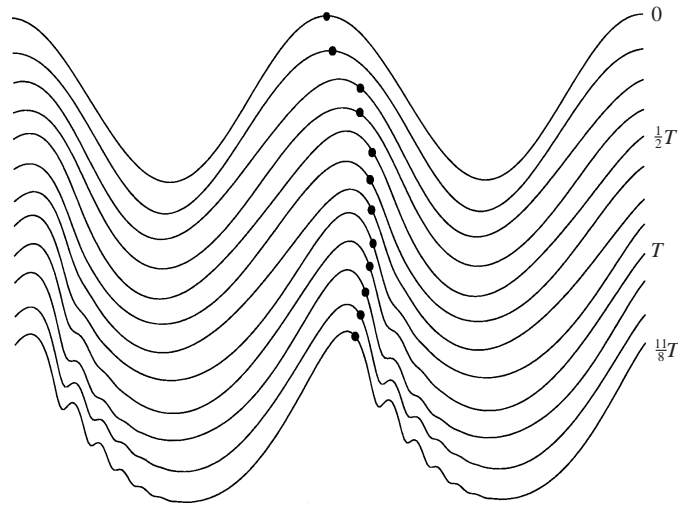
FIGURE 2. Ripple generation on 6.5 cm ($\kappa = 0.07$) waves simulated with a sinusoidal initial condition, an initial $ka = 0.20$, and $Re = \infty$. The time increment from top to bottom is $T/8$, and the frame of reference moves (left to right) with the linear phase speed. Dots represent the locations of maximum crest curvature. The vertical scale is exaggerated approxmiately 8:1.

steepness than their observations. As in Perlin *et al.* (1993), our attempts to find steady, asymmetric gravity–capillary waves failed. Therefore we propose that unsteadiness and the horizontal asymmetry of the underlying wave are responsible for some of the discrepancies and controversy discussed in LH95. In attempting to further verify this, we are naturally led to study in §4.2 different initial conditions and the dynamics of the underlying gravity waves.

4.2. *Nonlinear recurrence of crest asymmetry*

We again start the calculation with a sinusoidal wave and $ka = 0.20$, but now with zero surface tension. The most interesting feature in the subsequent wave motion (figure 3) is the crest pitching: the crest peaks and tilts forward initially to an asymmetric form, achieves a maximum steepness with a symmetric but sharper form, tilts backwards with a reduced steepness and asymmetry, and then resumes the symmetric form once again. The same sequence repeats after two wave periods, and is not qualitatively affected by the addition of damping. The two asymmetric crest forms alternate as the wave propagates from left to right for the entire inviscid simulation of 30 wave periods (approximately 210 000 time steps). The instantaneous maximum forward slope and backward slope are denoted by S_+ and S_- as shown in figure 4. The magnitudes of $|S_+|$ and $|S_-|$ oscillate between 0.15 and 0.28.

As we assume spatial periodicity, the modulation in figure 3 is not caused by the Benjamin–Feir instability, which can lead to a steepened and forward-tilting crest in an initially uniform wave train (Longuet-Higgins & Cokelet 1976). Bryant (1983) found a similar crest pitching motion in unsteady gravity waves with a similar period of $2T$ near $ka = 0.20$. Determined by enforcing temporal periodicity, the modulation period seems to become longer for larger wave steepness. This is also consistent with the nonlinear recurrence found in Dommermuth (1994) for gravity–capillary waves with parasitic ripples.

To understand the effect of crest pitching on parasitic ripple generation, we monitor the crest curvature and mark the maximum curvature by dots in figure 3. The crest
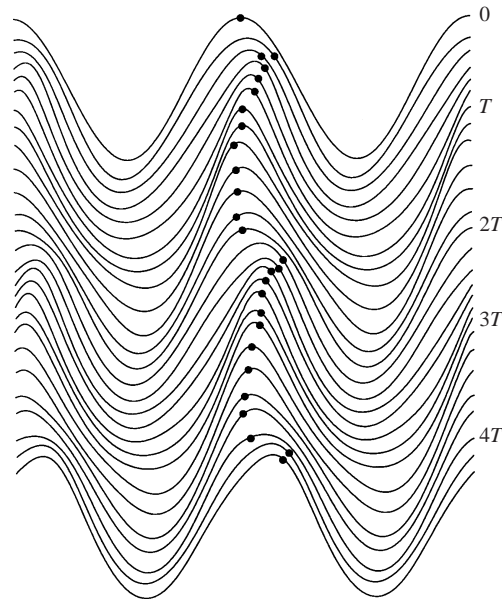
FIGURE 3. Gravity wave ($\kappa = 0$) profiles over four wave periods in a frame of reference moving (left to right) at the linear phase speed. The top profile is the sinusoidal initial wave with $ka = 0.20$. The profiles are separated by a time interval of $T/6$, $Re = \infty$. The vertical scale is exaggerated approximately 10:1.
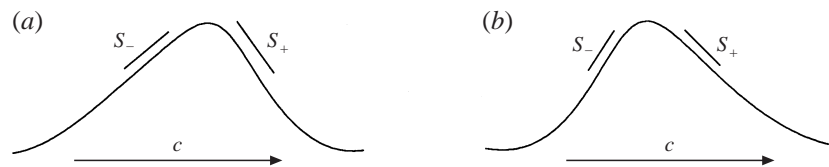

FIGURE 4. The two asymmetric crest forms in the previous figure:
(a) $|S_+| > |S_-|$; (b) $|S_+| < |S_-|$.

curvature increases substantially as the crest tilts forward, and its position shifts away from the maximum wave elevation. Note that the vertical scale in figure 3 is exaggerated. The crest curvature achieves a maximum of $\Gamma/k = 0.8$ when the crest becomes approximately symmetric (the seventh profile from the top), its value being approximately four times the crest curvature for the initial sinusoidal wave. For the symmetric Stokes waves of LH95, a crest curvature of 0.8 corresponds to $ka \approx 0.31$, significantly larger than $ka \approx 0.20$ in the unsteady wave of figure 3. Similarly, the ripple steepness in the experiments of Perlin *et al.* (1993) at $ka = 0.22$ is comparable with the quasi-steady solution of LH63 at $ka = 0.29$. However, this does not contradict the conclusion of LH63 and LH95 that the curvature-induced pressure is the source of parasitic ripples. Large crest curvature in the simulated unsteady wave leads to larger ripple steepness when surface tension is considered as in figure 2.

For pure gravity waves, the unsteadiness and the asymmetric crest pitching are largely dependent on the initial conditions. Using a third-order Stokes wave as an initial condition shows weaker crest asymmetry, and significantly reduces the maximum crest curvature (in time). Applying a fifth-order Stokes wave (Fenton 1985) as an initial condition almost eliminates the crest asymmetry and modulation
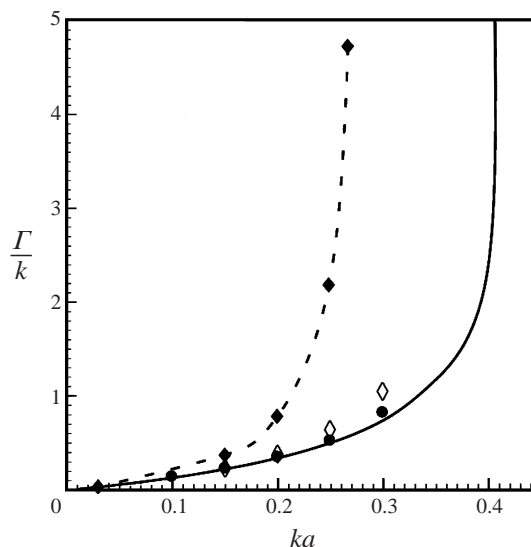
FIGURE 5. Maximum crest curvature Γ/k of unsteady gravity waves calculated with different initial conditions: -- ◆ --, linear wave; ◇, third-order Stokes wave; ●, fifth-order Stokes wave. ——, Crest curvature of fully nonlinear Stokes wave (LH95).

at moderate steepness. The crest curvature (figure 5) stays close to the Γ/k for steady Stokes waves (LH95) for all ka. For gravity–capillary waves, however, using initial conditions closer to the nonlinear Stokes waves does not eliminate the crest asymmetry. Our simulations still show strong parasitic ripples as explained in §4.3.

4.3. *Crest asymmetry and maximum ripple steepness*

In a study of Wilton ripples, Perlin & Ting (1992) observed significant differences between upstream and downstream wave slopes. Crest asymmetry is also demonstrated by Chang *et al.* (1978) for much longer gravity–capillary waves. We now show that it is almost ubiquitous in experiments on parasitic ripple generation. However, to date this effect on the ripple steepness has not been emphasized.

Slopes of a gravity–capillary wave and parasitic ripples are illustrated in figure 6. Similarly to the slope definition for gravity waves, S_-^0 is the maximum slope on the backward face of the primary wave crest (the 0th crest). S_+^0 represents the slope at the steepest point before the trough of the first ripple. When there are no ripples, $S_{+,-}^0$ are equivalent to $S_{+,-}$ defined earlier in figure 4. The ripple crests are denoted by $i = 1, \dots, n$, where n is the total number of ripples. For each ripple crest, the maximum slopes on the forward face and the backward face are represented by S_+^i and S_-^i, respectively. These value are easily calculated in our simulations. In the experiments, we measure ripple slopes from a curve fit of the spatial wave profile. The steepness of each ripple can be defined as

$$\theta^i = \frac{S_-^i - S_+^i}{2}, \quad i = 1, \dots, n.$$

The maximum ripple steepness θ_r is defined as the largest θ^i in both space (an entire wavelength) and time. The largest ripple during ripple generation is usually the first one on the forward face, i.e. $\theta_r = \theta^1$.

Table 1 summarizes the steepness ka, slopes $|S_+^0|$, $|S_-^0|$, and the corresponding
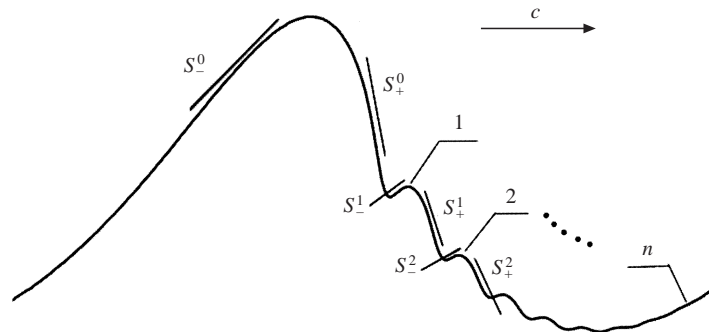
FIGURE 6. Definition of slopes on gravity–capillary waves with parasitic ripples. The primary wave crest is denoted by 0 and the ripple crests are denoted by $1, 2, \ldots, n$. S_+^i and S_-^i represent the maximum slopes on the forward and backward faces of each crest. Steepness of the ith ripple θ^i is defined as $(S_-^i - S_+^i)/2$.

	λ (cm)	ka	$|S_+^0|$	$|S_-^0|$	θ_r	Comments
Longuet-Higgins (1995)	6.8	0.227	0.23	0.23	0.07	Theory
	8	0.28	0.47	0.35	0.25	
Perlin *et al.* (1993)	6.8	0.22	0.39	0.23	0.17	Experiments with
	10.5	0.24	0.35	0.24	0.33	mechanical wavemaker
Zhang (1995)	7.5	0.21	0.65	0.25	0.54	6.8 m s^{-1} wind generated
	5	0.25	0.60	0.16	0.45	9.7 m s^{-1} wind generated
Dommermuth (1994)	5	0.22	0.42	0.22	0.24	Computation, $t = 3T$
	10	0.28	0.34	0.30	0.06	$t = 3T$
Mui & Dommermuth	5	0.28	1.12	0.25	0.54	Computation, $t = 2T$
Present (sinusoidal	6.5	0.20	0.57	0.22	0.20	Computation, $t = 2T$
initial condition)	5	0.20	0.61	0.26	0.38	$t = 2T$

TABLE 1. Horizontal asymmetry for parasitic ripple generation. λ, wavelength; ka, wave steepness; θ_r, maximum ripple steepness. Values cited for Zhang (1995) are measured from curve fits of the reported wave profiles.

θ_r from several studies on parasitic ripple generation. Slopes and ripple steepness are directly measured from the reported wave profiles. Experiments with insufficient information on θ_r and ka are excluded, such as Chang *et al.* (1978) and Ebuchi *et al.* (1987). Chang *et al.* (1978) further restricted their study to nearly symmetric wave profiles at certain locations.

The theory of Longuet-Higgins shows noticeable asymmetry only at larger wave steepness. Both experiments (Perlin *et al.* 1993; Zhang 1995) and numerical simulation (Dommermuth 1994) show significant asymmetry and larger ripple steepness at moderate ka. The crest asymmetry is more significant at shorter wavelengths. In the study of wind-generated ripples by Zhang (1995), the underlying wave is not strictly periodic in space and the ka values are at best an upper limit (see figure 12 therein). However, large $|S_+^0|$ and θ_r are observed at $ka = 0.21$. The large $|S_+^0|$ obtained in our simulation is very close to the spilling-breaker limit observed by Bonmarin (1989) for gravity waves. Local breaking may occur and cause numerical divergence mentioned

λ (cm)	Re	κ	ka	N_{min}	Δt_{min}	θ_r	λ_r (mm)	Γ/k	$|\Gamma_r|/k$
10	6286	0.029	0.30	512	0.0001	0.30	2.67	4.17	9.39
8	4498	0.045	0.28	256	0.001	0.38	2.80	2.93	7.64
			0.24	128	0.001	0.08	3.58	1.15	1.15
			0.20	128	0.001	0.02	3.88	0.51	0.38
7	3681	0.059	0.22	128	0.001	0.11	3.25	0.72	2.79
6	2921	0.081	0.21	128	0.001	0.17	3.88	0.76	3.63
5	2222	0.116	0.35	512	0.0001	1.53	3.75	10.35	27.06
			0.30	256	0.0002	1.03	3.72	4.85	25.47
			0.25	256	0.001	0.38	4.26	1.52	4.06
			0.20	128	0.001	0.22	4.69	0.88	2.79
			0.18	128	0.001	0.13	4.83	0.64	1.59
			0.15	128	0.005	0.11	5.00	0.40	0.64

TABLE 2. Summary of calculations for unsteady gravity–capillary waves and the obtained parameters for the parasitic ripples. Maximum ripple steepness θ_r, the maximum crest curvature Γ/k, and ripple curvature Γ_r/k represent the maximum value attained over time and space. The ripple wavelength λ_r is averaged over one primary wavelength. The Reynolds number Re and the inverse Bond number κ are defined in §2. Also listed are the minimum grid number necessary for spatial convergence N_{min} and the time step Δt_{min} (linear wave period: 2π).

in §4.1. Nonetheless, the crest asymmetry and large ripple steepness in our simulations are similar to the experimental results in table 1.

Better temporal convergence (longer time marching) is achieved when the higher-order wave solutions are applied as initial conditions, especially for shorter wavelengths. These include a third-order gravity–capillary wave solution (summarized in table 2) and a fifth-order Stokes wave solution. The calculated θ_r is smaller than that obtained with sinusoidal initial conditions, but is still larger than the quasi-steady prediction of LH95. The crest asymmetry remains pronounced. These results are similar to Dommermuth (1994) who applied a high-order expansion for a Stokes wave (Schwartz 1974) as the initial condition. Including the weak dissipation term in equation (2.2) usually only makes a small difference in the modelling of ripple formation. However, for larger ka values above 0.25, the added dissipation allows the computation to proceed past the initial transient maximum of ripple steepness and achieve the nearly steady decay of ripples (as in Dommermuth 1994). Similarly to the definition of θ_r, Γ_r/k in table 2 represents the maximum ripple curvature (usually in the trough) over both space and time.

In support of LH63, the ripple steepness increases with ka in table 2. The ripple wavelength λ_r does not heavily depend on the wavelength of the primary wave, but is strongly correlated with ka and the crest curvature Γ/k. On the ripple steepness, better agreement with LH95 is achieved for longer wavelengths ($\lambda = 8, 10$ cm) and our calculated θ_r is only slightly larger. The maximum crest curvature is significantly larger than that of a steady Stokes wave (see figure 5) even though higher-order solutions are used as initial conditions. Figure 7 shows the forward-tilting crest when the ripples reach the maximum steepness during their growth. Our computation for $\lambda = 10$ cm and $ka > 0.30$ diverges before a definite θ_r can be obtained. This computational difficulty represents local breaking and the breakdown in the quasi-potential flow formulation.

Another interesting prediction of LH95 is the subcritical and supercritical phenomena described below. Wave-generated ripples experience an effective gravitational

(a) $\lambda = 6$ cm

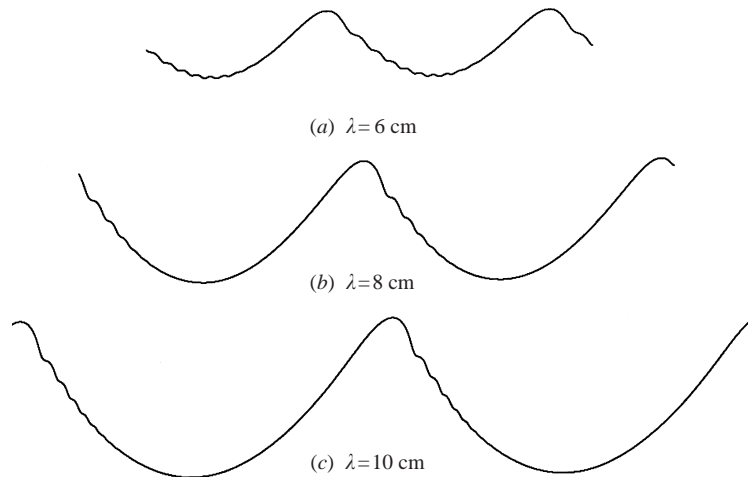(b) $\lambda = 8$ cm

(c) $\lambda = 10$ cm

FIGURE 7. The simulated wave profiles when the maximum ripple steepness is observed. (a) $\lambda = 6$ cm, $ka = 0.21$, $|S_+^0| = 0.38$, $|S_-^0| = 0.21$; (b) $\lambda = 8$ cm, $ka = 0.28$, $|S_+^0| = 0.73$, $|S_-^0| = 0.30$; (c) $\lambda = 10$ cm, $ka = 0.30$, $|S_+^0| = 0.88$, $|S_-^0| = 0.34$. Two wavelengths are shown and the vertical scale is exaggerated by 4.

acceleration $g^* = g\cos\theta - \Gamma q^2$, which includes the normal component of gravity and the centrifugal acceleration arising from the surface current q and the surface curvature Γ. Capillary waves develop only when q exceeds the minimum phase speed of capillary–gravity waves, $c_{min} = (4g^*\sigma)^{1/4}$. This condition is satisfied everywhere on the underlying wave when Γ/k is small and the wave is subcritical. For steep gravity waves where Γ/k is locally large at the crest, the surface current q is less than c_{min} near the crest and ripples are then blocked by two caustics determined by $q = c_{min}$. Therefore the ripple steepness increases with increasing ka for subcritical waves, but starts to decrease once ka surpasses ka_{cr} (see figures 12 and 13 of LH95). The first ripple merges with the primary gravity-wave crest because of the blocking effect. The critical steepness ka_{cr} for the blocking to occur is 0.34, 0.31, and 0.19 for 10 cm, 8 cm, and 5 cm wavelengths respectively.

Our calculations for $\lambda = 5$ cm cover a wide range of ka and therefore facilitate verification of the critical steepness mentioned above. In figure 8, these results are compared with measurements from Yermakov *et al.* (1986), computations from Dommermuth (1994), and some new experimental data. We emphasize that θ_r shown here is a transient value different from that defined in LH63 and LH95. The calculated θ_r is significantly larger than the prediction of LH95, but is in reasonable agreement with Yermakov *et al.* and Dommermuth. At $ka = 0.20$, Yermakov *et al.* measured larger θ_r, while the computations of Dommermuth show slightly smaller ripples than our numerical results. Recall that blocking should occur at $ka_{cr} = 0.19$. However, both our calculations and the experiments by Yermakov *et al.* (1986) show continuously increasing θ_r above $ka_{cr} = 0.19$. The same monotonic increase is also indicated elsewhere in the calculation by Dommermuth for $\lambda = 8$ cm (see Longuet-Higgins 1996). Therefore, the unsteadiness may significantly reduce ripple blocking.† The calculated wave profiles are shown in figure 9.

† In the calculation of Fedorov & Melville (1998) for gravity–capillary waves with wind forcing, steepness of the capillary ripples also increases monotonically with the underlying wave steepness until wave breaking.
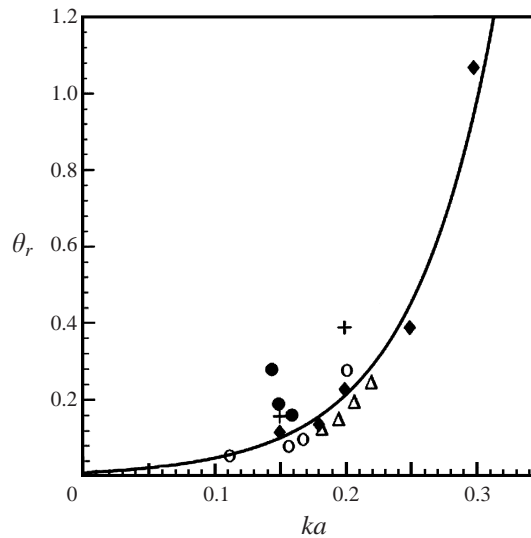
FIGURE 8. The maximum ripple steepness θ_r from our simulation and previous experiments for 5 cm waves. The solid line is a polynomial fit of our numerical data; ◆, data cited in table 2; +, calculated results when sinusoidal initial conditions are applied; ○, measurements from Yermakov *et al.* (1986); △, numerical results of Dommermuth (1994); ●, new experimental data shown in §5.
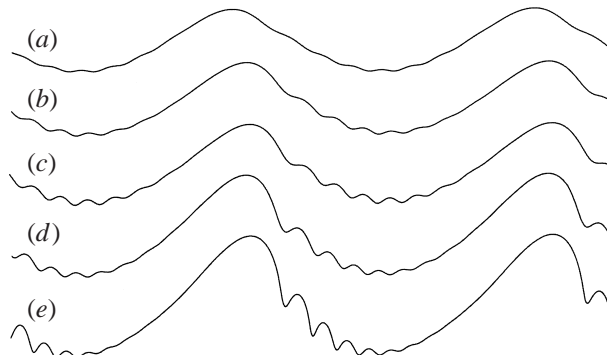

FIGURE 9. Simulated 5 cm waves with the maximum ripple steepness shown in figure 8. The initial ka is (*a*) 0.15, (*b*) 0.18, (*c*) 0.20, (*d*) 0.25, (*e*) 0.30. The vertical scale is exaggerated by 4:1.

Three experimental measurements shown in figure 8 suggest significantly larger θ_r than our calculations at $ka \approx 0.15$. The ripple steepness also decreases rapidly with a slight increase of ka in the experiments. This decreasing trend is not due to the effect of steep-wave blocking. It only shows that unsteady ripples are very sensitive to the underlying crest asymmetry (see §5.3). Our computations with sinusoidal initial conditions ($ka = 0.15$ and 0.20) also show larger ripple steepness. This demonstrates that the parasitic ripples are also sensitive to the unsteadiness of the underlying wave.

4.4. *Parasitic ripple evolution*

We have shown in §4.2 that gravity waves, with finite initial perturbation, exhibit a 'pitching' crest motion and alternating asymmetry in wave slope. If the asymmetric crest is unaffected by small capillary ripples (no strong feedback), the modulation in crest shape should lead to modulations of ripple steepness too.
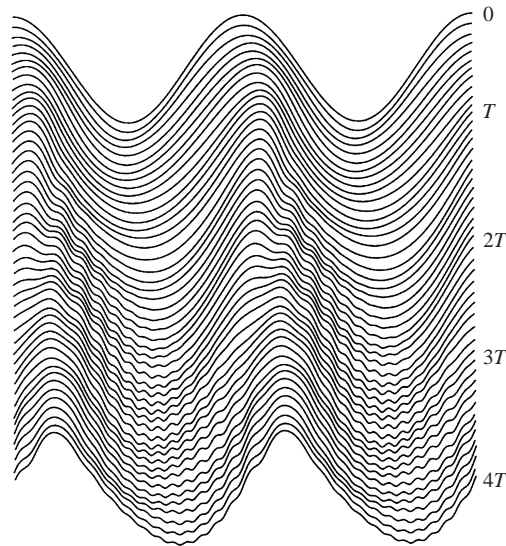
FIGURE 10. Simulated 6.5 cm wave with $T/12$ time interval in a moving coordinate at the linear wave speed (from left to right). $t = 0–4T$, $ka = 0.15$, $Re = 3294$. The vertical scale is exaggerated.

Indeed, alternating crest asymmetries exist when surface tension is included in the simulations, but crest–ripple interaction is significant. Figure 10 shows 6.5 cm waves in a coordinate moving with the linear phase speed. Relative to a fixed coordinate, the wave moves from left to right. Initially, the wave assumes a sinusoidal profile with $ka = 0.15$. It travels faster than its linear speed as expected, but in a unique fashion: the crest tilts forward initially and ripples appear on the forward face. When the crest starts tilting backward after two wave periods (the 30th profile from the top), a new crest emerges from the first ripple on the forward face as if the crest were 'shifting' forward abruptly. Note that in the simulation without surface tension, the crest tilts forward again after $2T$ (figure 3). The parasitic ripples eventually reach the backward face of the next crest. This ripple generation process is significantly different from previous experimental studies where only forward-tilting crests are reported.

The interaction between the primary wave crest and the first ripple persists even for longer time calculations: it would appear that the ripples are strongest in the wave trough while the crest follows the same 'shifting' motion shown in figure 10. Here, the crest–ripple interaction is caused by the alternating crest asymmetry, not by the blocking effect of the steep underlying wave as suggested in LH95. When third-order gravity–capillary waves are applied as the initial condition, asymmetry and the crest–ripple interaction are subdued. The maximum crest elevation still shifts between two positions at the edge of the crest in later stages. Significant ripples are observed in the wave trough as in the steady solution found by Schwartz & Vanden-Broeck (1979). Experiments for 5 cm wavelength show similar large ripples in the trough (§ 5.3) although experiments for longer wavelengths show significant ripples mostly near the wave crest. In § 5.5, we will discuss experiments with a crest-shifting motion very similar to that in figure 10.

5. Experimental results

The large ripple steepness demonstrated in Perlin *et al.* (1993) was suspected by LH95 to be caused by the mechanical method of wave generation. The plunging

Frequency (Hz)	λ_l (cm)	λ_m (cm)	c (cm s^{-1})	ka
4.21	9.0	10.1	43	0.25–0.11
4.87	7.0	7.5–7.2	36	0.22–0.08
5.26	6.0	6.7–6.5	35	0.21–0.10
6.10	4.7	5.1–4.8	30	0.15–0.03
6.70	4.1	5.0–4.1	—	0.16–0.13

TABLE 3. The frequency, the wavelength (the linear estimate is λ_l and the measured value is λ_m), the approximate phase speed c, and the underlying wave steepness ka for experiments. The λ and ka ranges are based upon measurements between 15 cm and 60 cm downstream from the wavemaker for different wavemaker strokes.

wavemaker in Perlin *et al.* (1993) can have a 'pumping' effect – water on the back of the wavemaker is transported in the wave direction and produces additional drift and vorticity. However, the ripple steepness examined here is comparable to Perlin *et al.* (1993) even though we adopt a flapping wavemaker and the 'pumping' effect is not present. We recognize that using a rigid wavemaker does not reproduce the particle velocity given by a Stokes wave. Therefore the generated wave, with or without surface tension, is different from the Longuet-Higgins gravity-wave solution. Nonetheless, significant ripples at moderate ka appear in studies on wind-wave fields and in our and Dommermuth's (1994) time-marching computations. Hence, large unsteady ripples are not merely an artifact of the mechanical method of wave generation.

Five sets of experiments are conducted with different wavemaker frequencies: 4.21 Hz, 4.87 Hz, 5.26 Hz, 6.10 Hz, and 6.70 Hz. The corresponding wavelengths range from about 4 cm to 10 cm as shown in table 3. Because of the wave nonlinearity, the measured wavelength at a particular frequency is longer than the wavelength estimated from linear wave theory. Each frequency set consists of measurements for observation windows moving at approximately the wave phase speed. Three wavemaker stroke amplitudes are applied to generate different wave amplitudes. We limit the wavemaker stroke to avoid local breaking and turbulent motion around the wavemaker so that the generated wave profiles remain two-dimensional for all reported experiments.

The wave amplitude decays significantly between 15 cm and 60 cm downstream from the wavemaker due to the enhanced damping during ripple generation. As this has been discussed in detail in previous studies (Perlin *et al.* 1993), we will focus on the ripple evolution and the correlation between underlying wave motion and ripple steepness. The latter is determined from a least-square curve fit of the elevation profile, its value approximated by one half of the difference between the maximum (positive) and the minimum (negative) ripple slope. The maximum ripple steepness usually occurs on the forward face on the ripple closest to the primary wave crest.

5.1. *4.87 Hz experiments*

Two small wavemaker strokes produce wave steepness of $ka = 0.16$ and $ka = 0.19$ at a distance 21 cm (three wavelengths) from the wavemaker. Figure 11(*a*) shows obvious ripples on the forward face and a slightly asymmetric crest for $ka = 0.16$. The ripple steepness is slightly smaller in figure 11(*b*) even though $ka = 0.19$ is larger and the crest appears to be sharper. In both cases, the largest ripple steepness appears near the crest. There is slight temporal oscillation in the primary wave amplitude and the ripples are quasi-steady at this location. Following the wave crest downstream (not shown) leads to an almost monotonic temporal decay of the ripples. The ripples
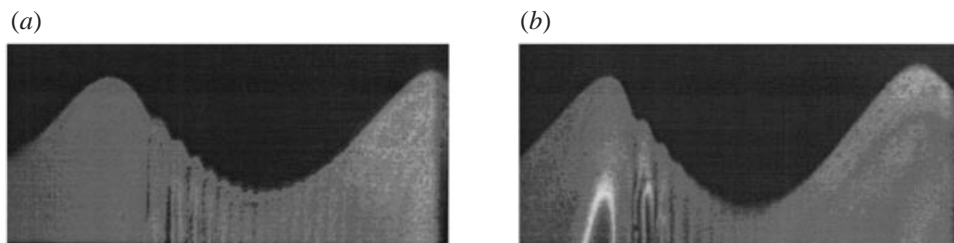
(*a*)   (*b*)

FIGURE 11. Gravity–capillary waves of 4.87 Hz ($\lambda = 7.5$ cm) with (*a*) $ka = 0.16$, (*b*) $ka = 0.19$.
The image centre is located about 21 cm downstream from the wavemaker.

become much smaller 30 cm downstream such that their existence is only verified by the intensity variation of the laser sheet in the water column due to surface curvature variation. These qualitative features are essentially in agreement with LH63.

The waves presented in figure 12 with $ka = 0.21$ are produced by a larger wavemaker stroke. As in the computational results of figure 10, the reference frame moves downstream at the approximate phase velocity to follow the individual wave crest (as for all the experiments). The capillary ripples appear to be phase-locked to the crest and their amplitude decays spatially along the forward face of the primary wave. Approximately, eight capillary ripples can be distinguished in the first frame recorded 21 cm from the wavemaker. Large spatial/temporal modulation of the primary wave crests is evident, resulting in temporally modulated ripples (from 12 ms to 42 ms). In figure 12(*a*), the upstream crest and the downstream crest have local steepness ka of 0.18 and 0.22, respectively. After a quarter wave period (figure 12*h*), the upstream crest achieves a local steepness of $ka = 0.23$. This spatial modulation resembles the Benjamin–Feir instability studied by Longuet-Higgins & Cokelet (1976) for gravity wave trains. The ripple steepness at 48 ms and 54 ms is much less than that at 0 ms even though the local steepness is 25% larger. Besides viscous dissipation, the primary reason for the reduced ripple steepness is the more symmetric crest in figure 12(*i, j*). We will discuss this effect further in the following sections.

5.2. *5.26 Hz experiments*

Figure 13 shows two 6.5 cm waves generated by two different forcing strokes, moving left to right. Although a larger forcing stroke does not increase ka of the wave in figure 13(*b*), the primary wave crest (upstream) is more asymmetric than that in figure 13(*a*). Accordingly, the ripple steepness is larger in figure 13(*b*), and the spatial modulation is more evident. Both images are obtained approximately three wavelengths (18 cm) downstream and should be free of the evanescent modes directly generated by the wavemaker. It is worth noting that the downstream wave of figure 13(*b*) has a backward-tilting crest ($|S_-^0| > |S_+^0|$), similar to our numerical finding (figure 4).

Figure 14 presents very steep ripples for $ka = 0.21$. There are at least 14 ripples per wavelength at 0 ms, more than the number exhibited by the 4.87 Hz waves at similar ka. Ripples are also present on the leeward surface of the second crest. The ripple wavelengths decrease from the first ripple (in front of the wave crest) to those in the trough, but increase again for those on the leeward face. Similar results are observed in our calculations (e.g. figure 10).

At this frequency, the parasitic ripples also appear nearly phase-locked to the underlying wave. Their steepness, however, is strongly modulated in time due to the unsteady motion of the underlying wave. This is the same modulation shown earlier
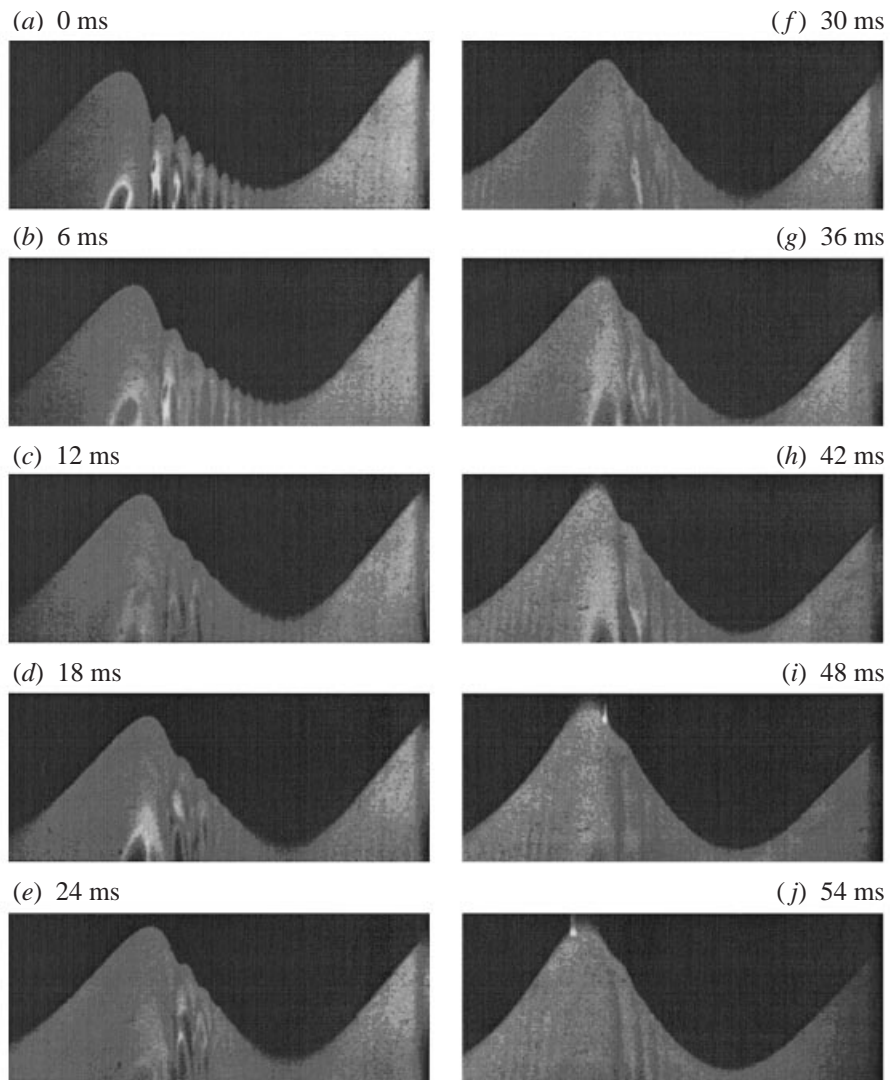
(*a*) 0 ms

(*f*) 30 ms

(*b*) 6 ms

(*g*) 36 ms

(*c*) 12 ms

(*h*) 42 ms

(*d*) 18 ms

(*i*) 48 ms

(*e*) 24 ms

(*j*) 54 ms

FIGURE 12. Gravity–capillary waves of 4.87 Hz with an average $ka = 0.21$. The images are recorded following the underlying wave crest moving left to right.
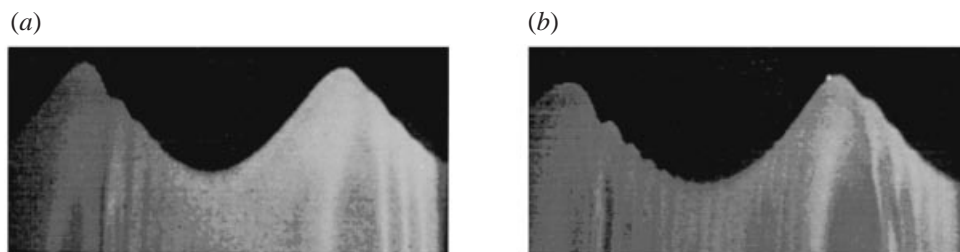
(*a*)

(*b*)

FIGURE 13. Gravity–capillary waves of 5.26 Hz at the instant of maximum ripple steepness, both recorded about 18 cm downstream: (*a*) smallest forcing stroke, $ka = 0.19$, (*b*) larger forcing stroke, $ka = 0.18$.
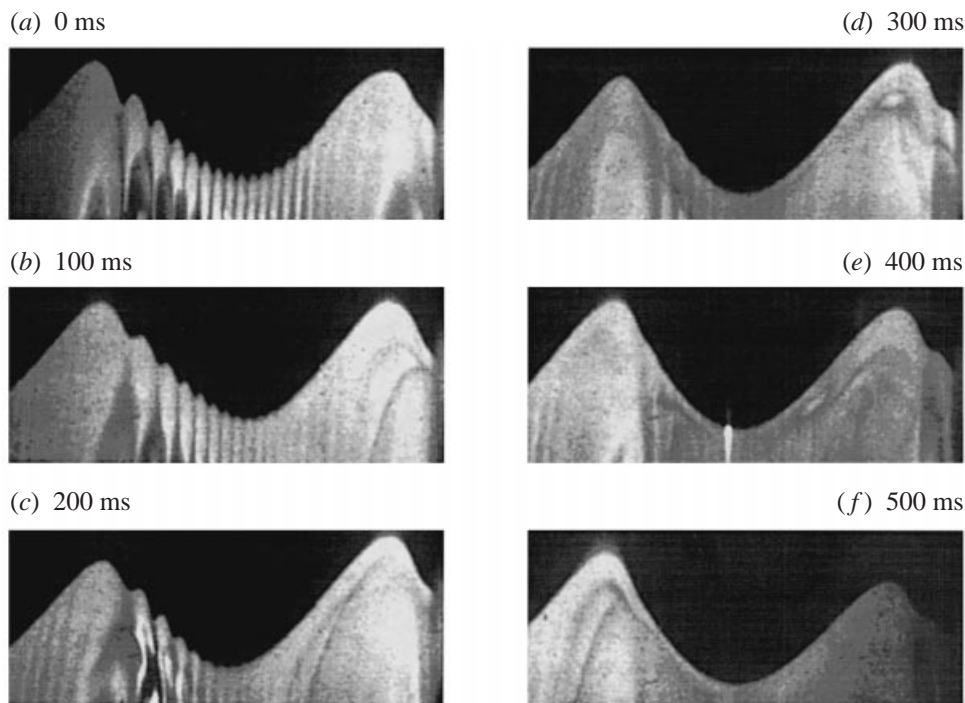
(*a*) 0 ms

(*d*) 300 ms

(*b*) 100 ms

(*e*) 400 ms

(*c*) 200 ms

(*f*) 500 ms

FIGURE 14. A sequence of 5.26 Hz waves following the underlying wave crest from (*a*) 18 cm to (*f*) 33 cm downstream of the wavemaker with approximately 3 cm intervals (average $ka = 0.21$).

for 4.87 Hz waves. Initially, the two crests shown in figure 14 are of equal amplitudes. But after 0.2 s, the downstream crest increases, and the upstream crest settles down (figure 14*c*). The rising downstream crest seems to block the ripples and increase the ripple steepness on the upstream crest as compared with figure 14(*b*). This seems to be a transitory effect due to spatial modulation not captured by either our calculation or LH95. The upstream crest rises again and tilts forward at 0.4 s, but now the ripple presence can only be verified by the refracted laser light in the water.

5.3. *6.10 Hz experiments*

Figure 15(*a*) shows the calculated 5 cm wave at the time of maximum ripple steepness starting from sinusoidal initial conditions. The subsequent ripple motion in our calculation is very similar to that of the 6.5 cm waves in figure 10 and therefore is not shown here. Figure 15(*b–f*) presents waves recorded by following the wave crest downstream in the experiments. Initially, the four capillary ripples evident on the forward face of the primary wave appear to be phase-locked with the crest (figure 15*b*). Both the ripple steepness and the number of ripples agree with the numerical profile. After travelling 5 cm downstream, the ripples are greatly reduced, and appear to approach the quasi-steady state described by LH63.

Many features of the 6.10 Hz waves are similar to the 4.87 Hz waves and the 5.26 Hz waves shown previously. For example, the maximum ripple steepness is strongly affected by the unsteady motion of the primary wave. Because of the short wavelength, the 6.10 Hz waves have strong ripples in the trough of the underlying wave (upstream in figure 15*d* and *e*). This agrees with our simulation in figure 10 where the crest modulation is accompanied by strong ripples in the wave trough.
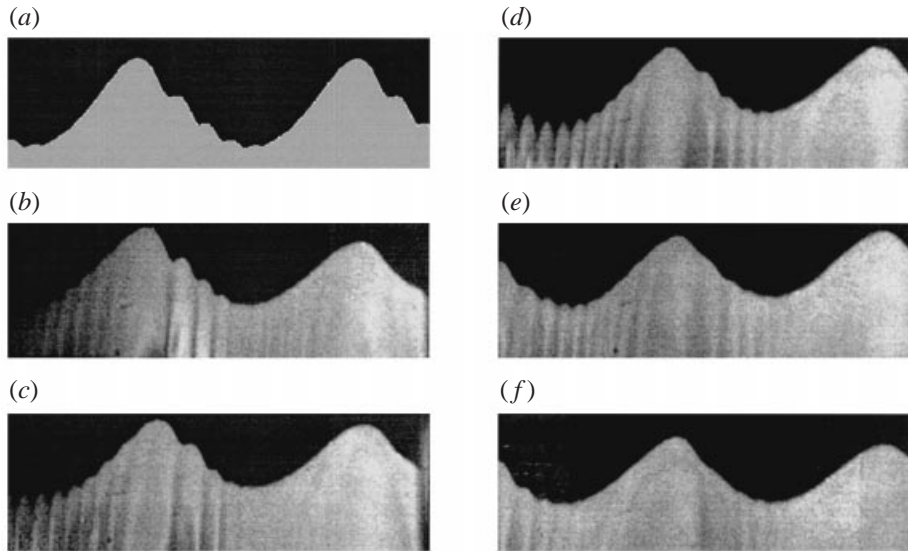
FIGURE 15. (*a*) The calculated 5 cm wave at the instant of maximum ripple steepness with $ka = 0.15$, (*b*–*f*) experimental profiles of 6.10 Hz waves ($\lambda = 5$ cm, $ka = 0.15$) at 15 cm, 16.5 cm, 18 cm, 19.5 cm, and 21 cm from the wavemaker following the wave crest.

Data for all three wavelengths with ka between 0.15 and 0.21 (where the theory of LH95 predicts a quasi-steady state with very small ripple steepness) show significant ripples that do not necessarily increase with larger wave steepness. We instead find a correlation between ripple steepness and the crest asymmetry. The trend is demonstrated in table 4 and figure 16. For comparison, we choose the wave profiles recorded at three wavelengths downstream for each forcing frequency. Three different wave steepness presented for each frequency are obtained with three different wavemaker strokes. For each frequency listed in table 4, the small variations in the wave steepness correspond to a large range of ripple steepness. Some of the data are already shown in figures 11, 12(*a*), 13, 14(*a*), 15(*b*). The chosen crest is on the left of the image with slight variations in its location. The degree of crest asymmetry is represented by $|S_+^0/S_-^0|$, a ratio between the forward and backward crest slopes. There is a qualitative correlation between increasing ripple steepness θ_r and increasing crest asymmetry at moderate wave steepness.

5.4. *6.70 Hz experiments*

For the highest frequency experiment reported here, the wave decays very quickly and its amplitude is very small after propagating 30 cm downstream. Hence only waves 15 cm downstream are studied. Using different wavemaker strokes we obtain $ka = 0.16$, 0.14, and 0.13 with 5.0 cm, 4.4 cm, and 4.1 cm wavelengths, respectively. Internal resonance between the capillary ripples and the underlying wave becomes more significant for these waves and six ripples are observed along the entire wave-length with comparable steepness. Weakly nonlinear theory predicts sixth-harmonic resonance at 6.59 Hz and fifth-harmonic resonance at 6.99 Hz, both studied by McGoldrick (1972). Compared to lower frequency waves, the ripples are not phase-locked to the wave crest but still decay monotonically downstream. The wave crest is often overtaken by the closest ripple on the backward face similar to the crest modulation shown in our numerical simulation (figure 10). Since both the length and height scales

Frequency f (Hz)	$\overline{ka}$	$|S_+^0|$	$|S_-^0|$	$|S_+^0/S_-^0|$	θ_r
4.87	0.16	0.26	0.16	1.7	0.18
	0.19	0.31	0.16	1.9	0.16
	0.21	0.72	0.18	4.0	0.46
5.26	0.19	0.30	0.21	1.4	0.14
	0.18	0.40	0.14	2.9	0.22
	0.21	0.49	0.16	3.2	0.37
6.10	0.15	0.46	0.10	4.6	0.27
	0.15	0.32	0.13	2.6	0.18
	0.16	0.27	0.13	2.2	0.15

TABLE 4. Maximum ripple steepness θ_r and the crest slopes, $|S_+^0|$ and $|S_-^0|$ for the experimental wave profiles measured three wavelengths downstream from the wavemaker. At each frequency, the three waves correspond to three different forcing strokes. The time-averaged wave steepness at this location is represented by $\overline{ka}$.
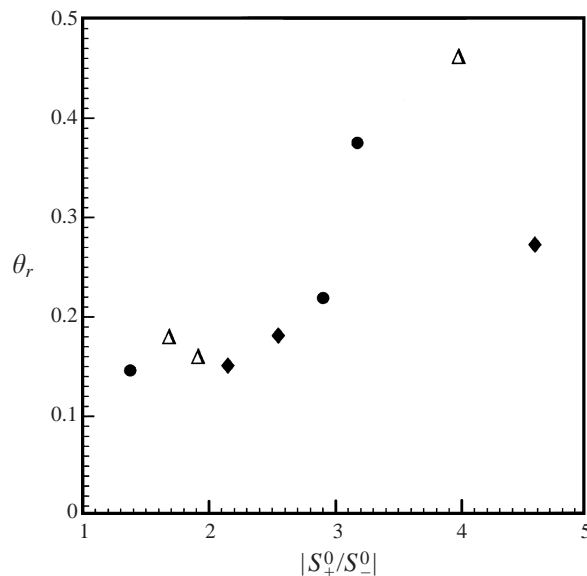

FIGURE 16. Correlation between measured maximum ripple steepness θ_r and the degree of crest asymmetry $|S_+^0/S_-^0|$. ◆, $f = 6.10\,\mathrm{Hz}$; ●, $f = 5.26\,\mathrm{Hz}$; △, $f = 4.87\,\mathrm{Hz}$.

of these ripples are closer to those of the underlying wave, the phenomenon is more reminiscent of a ripple and a crest merging.

5.5. *4.21 Hz experiments*

The longest waves measured in our experiments show significant ripple recurrence at moderate wave steepness. Capillary ripples are visible for $ka > 0.13$. The average ka of the two primary waves is 0.24 in figure 17. Here we extract the wave profiles using an edge detection scheme and overlap the images in a reference frame following the crest. Amplitudes of the ripples are greatest near the crests of the primary wave and decay along the forward surface of the underlying wave. Approximately 12 ripples
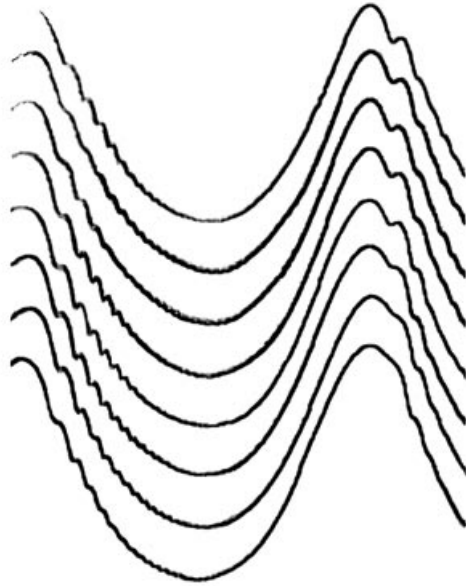
FIGURE 17. 4.21 Hz waves with ripple modulation close to the upstream crest and crest–ripple interaction near the downstream crest, $ka = 0.24$. Edge-detected profiles following the wave crest from 15 cm to 18.5 cm downstream.

are visible from the crest to the trough. These waves are measured from 15 cm to 18.5 cm downstream (at 0.5 cm intervals).

For the upstream (left) crest, modulation in the ripple steepness occurs over one wavelength: the ripple amplitude decreases to a minimum (approximately) half a wavelength downstream, and then increases again. The increase in ripple amplitude from the first to the last profile in figure 17 is accompanied by steepening of the forward face. This modulation is fairly repeatable when the wave train is generated by the same wavemaker driving signal. The slight underlying wave modulation has a similar period and therefore may cause the ripple modulation. Similar recurrence cannot be modelled in our numerical simulation domain.

Our numerical results in figure 10, however, exhibit a phenomenon very similar to the downstream crest in figure 17. Modulations in the underlying wave again cause ripple modulation, but the primary crest overtakes the first ripple as it propagates downstream. In the last profile of figure 17, the first ripple cannot be distinguished from the flatter crest. The downstream crest form in the fifth to the last profiles has striking similarity with figure 13 of LH95. However, the quasi-steady solution of LH95 has a much larger wave steepness where our calculation indicates local breaking. The merging of the largest ripple and the primary wave crest in figure 17 is more likely to be due to the unsteady effect that causes crest shifting in figure 10.

6. Concluding remarks

Our time-marching simulations demonstrate that large initial perturbations enhance ripple development and even cause local breaking. The crest asymmetry and large crest curvature during the gravity wave modulation are the most pronounced features of the ripple generation and contribute to large ripples at moderate underlying wave steepness. In contrast, viscous effects modelled by a viscous correction in the free-surface

conditions have less influence on the ripple generation. With appropriate initial conditions, the calculated maximum ripple steepness agrees reasonably well with previous calculations of Dommermuth (1994) and experiments by Yermakov *et al.* (1986).

Generated by a flap-type wavemaker, the experimental wave profiles with moderate *ka* show monotonically decaying waves with significant parasitic ripples. Following an individual wave crest reveals slight modulation in the primary wave (possibly due to Benjamin–Feir instability) and the corresponding ripple modulation. Large modulation of the underlying waves can even cause backward-tilting crests. At fixed locations, experiments show a direct correlation between large crest asymmetry and significant ripple generation at moderate wave steepness. Experiments for 4.21 Hz and 6.70 Hz waves and our numerical simulations demonstrate unsteady 'crest shifting' motions where the wave crest merges with the first ripple on the forward face. These characteristics may have significant implications for ripple generation on open seas with and without wind.

It is worth mentioning that we have investigated the possibility of (sub-) super-critical parasitic ripple generation. Our computations for unsteady 5 cm waves, however, demonstrate that the maximum ripple steepness increases monotonically with the underlying wave steepness. Therefore the blocking effect as predicted by LH95 may be limited to quasi-steady conditions.

REFERENCES

BONMARIN, P. 1989 Geometric properties of deep-water breaking waves. *J. Fluid Mech.* **209**, 405–433.

BRYANT, P. J. 1983 Cyclic gravity waves in deep water. *J. Austral. Math. Soc.* B **25**, 2–15.

CHANG, J. H., WAGNER, R. N. & YUEN, H. C. 1978 Measurement of high frequency capillary waves on steep gravity waves. *J. Fluid Mech.* **86**, 401–413.

CHEN, B. & SAFFMAN, P. G. 1979 Steady gravity–capillary waves on deep water I. Weakly nonlinear waves. *Stud. Appl. Maths* **60**, 183–210.

CHEN, B. & SAFFMAN, P. G. 1980 Steady gravity–capillary waves on deep water II. Numerical results for finite amplitude. *Stud. Appl. Maths* **62**, 95–111.

COX, C. S. 1958 Measurements of slopes of high-frequency wind waves. *J. Mar. Res.* **213**, 95–109.

DOMMERMUTH, D. G. 1994 Efficient simulation of short and long-wave interactions with applications to capillary waves. *Trans. ASME J. Fluids Engng* **116**, 77–82.

DUNCAN, J. H., PHILOMIN, V., BEHRES, M. & KIMMEL, J. 1994 The formation of spilling breaking water waves. *Phys. Fluids* **6**, 2558–2560.

EBUCHI, N., KAWAMURA, H. & TOBA, Y. 1987 Fine structure of laboratory wind-wave surfaces studied using an optical method. *Boundary-Layer Met.* **39**, 133–151.

FEDOROV, A. V. & MELVILLE, W. K. 1998 Nonlinear gravity–capillary waves with forcing and dissipation. *J. Fluid Mech.* **354**, 1–42.

FENTON, J. D. 1985 A fifth-order Stokes theory for steady waves. *ASCE J. Waterway, Port, Coastal Ocean Engng* **111**, 216–234.

JIANG, L., SCHULTZ, W. W. & PERLIN, M. 1996 Parasitic capillary waves and Wilton's ripples under Faraday resonance. *Bull. Am. Phys. Soc.* **41**, 1769.

LIN, H. J. & PERLIN, M. 1999 The velocity and vorticity fields beneath gravity–capillary waves exhibiting parasitic ripples. *Phys. Fluids* (submitted).

LONGUET-HIGGINS, M. S. 1963 The generation of capillary waves by steep gravity waves. *J. Fluid Mech.* **16**, 138–159 (referred to herein as LH63).

LONGUET-HIGGINS, M. S. 1978 The instabilities of gravity waves of finite amplitude in deep water. II. Subharmonics. *Proc. R. Soc. Lond.* A **360**, 489–505.

LONGUET-HIGGINS, M. S. 1992a Theory of weakly damped Stokes waves: a new formulation and its physical interpretation. *J. Fluid Mech.* **235**, 319–324.

LONGUET-HIGGINS, M. S. 1992b Capillary rollers and bores. *J. Fluid Mech.* **240**, 659–679.

LONGUET-HIGGINS, M. S. 1995 Parasitic capillary waves: a direct calculation. *J. Fluid Mech.* **301**, 79–107 (referred to herein as LH95).

LONGUET-HIGGINS, M. S. 1996 Progress towards understanding how waves break. Invited lecture, *The 21st Symposium on Naval Hydrodynamics*, pp. 7–28.

LONGUET-HIGGINS, M. S. & COKELET, E. D. 1976 The deformation of steep surface waves on water: I. A numerical method of computation. *Proc. R. Soc. Lond.* A **350**, 1–26.

LONGUET-HIGGINS, M. S. & CLEAVER, R. P. 1994 Crest instabilities of gravity waves. Part 1. The almost-highest wave. *J. Fluid Mech.* **258**, 115–129.

LONGUET-HIGGINS, M. S., CLEAVER, R. P. & FOX, M. J. H. 1994 Crest instabilities of gravity waves. Part 2. Matching and asymptotic analysis. *J. Fluid Mech.* **259**, 333–344.

LUNDGREN, T. S. 1989 A free-surface vortex method with weak viscous effects. *Mathematical Aspects of Vortex Dynamics* (ed. R. E. Caflisch), pp. 68–79.

McGOLDRICK, L. F. 1972 On the rippling of small waves: a harmonic nonlinear nearly resonant interaction. *J. Fluid Mech.* **42**, 725–751.

MIKSIS, M., VANDEN-BROECK, J.-M. & KELLER, J. B. 1982 Rising bubbles. *J. Fluid Mech.* **123**, 31–41.

MUI, R. C. Y. & DOMMERMUTH, D. G. 1995 The vortical structure of parasitic capillary waves. *Trans. ASME J. Fluids Engng* **117**, 355–361.

PERLIN, M., LIN, H. & TING, C.-L. 1993 On parasitic capillary waves generated by steep gravity waves: an experimental investigation with spatial and temporal measurements. *J. Fluid Mech.* **255**, 597–620.

PERLIN, M. & TING, C.-L. 1992 Steep gravity–capillary waves within the internal resonance regime. *Phys. Fluids* A **4**, 2466–2478.

PHILLIPS, O. M. 1981 The dispersion of short wavelets in the presence of a dominant long wave. *J. Fluid Mech.* **107**, 465–485.

SCHULTZ, W. W., HUH, J. & GRIFFIN, O. M. 1994 Potential energy in steep and breaking waves. *J. Fluid Mech.* **278**, 201–228.

SCHULTZ, W. W., VANDEN-BROECK J. M., JIANG, L. & PERLIN, M. 1998 Highly nonlinear standing water waves with small capillary effect. *J. Fluid Mech.* **369**, 253–272.

SCHWARTZ, L. W. 1974 Computer extension and analytic continuation of Stokes' expansion for gravity waves. *J. Fluid Mech.* **62**, 553–578.

SCHWARTZ, L. W. & VANDEN-BROECK, J.-M. 1979 Numerical solutions of the exact equations for capillary-gravity waves. *J. Fluid Mech.* **95**, 119–139.

SHYU, J. H. & PHILLIPS, O. M. 1990 The blockage of gravity and capillary waves by longer waves and currents. *J. Fluid Mech.* **217**, 115–141.

VINJE, T. & BREVIG, P. 1981 Numerical simulation of breaking waves. *Adv. Water Resources* **4**, 77–82.

WATSON K. M. & BUCHSBAUM, S. B. 1996 Interaction of capillary waves with longer waves. Part 1. General theory and specific applications to waves in one dimension. *J. Fluid Mech.* **321**, 87–120.

WEHAUSEN, J. V. & LAITONE, E. V. 1960 Surface waves. *Encyclopedia of Physics* IX, pp. 653–660. Springer.

WILTON, J. R. 1915 On ripples. *Phil. Mag.* **29**, 688–700.

WOODRUFF, S. L. & MESSITER, A. F. 1994 A perturbation analysis of an interaction between long and short surface waves. *Stud. Appl. Maths* **92**, 159–189.

YERMAKOV, S. A., RUVINSKY, K. D., SALASHIN, S. G. & FREIDMAN, G. I. 1986 Experimental investigation of the generation of capillary–gravity ripples by strongly nonlinear waves on the surface of a deep fluid. *Izv. Atmos. Ocean Phys.* **22**, 835–842.

ZHANG, X. 1995 Capillary–gravity and capillary waves generated in a wind wave tank: observations and theories. *J. Fluid Mech.* **289**, 51–82.